Electronic Supplementary Material (ESI) for ChemComm.

Supplementary Information

Developing dynamic magnetic flux template to mass production of 1D materials in a few minutes

*Yanjing Liang, Zhiqing Zhu, Qi Li, Qingsong Huang**

School of Chemical Engineering, Sichuan University, Chengdu 610065, China.

E-mail: qshuang@scu.edu.cn

1. The DMT provides a template for Ga_2O_3 nanoribbons' growth

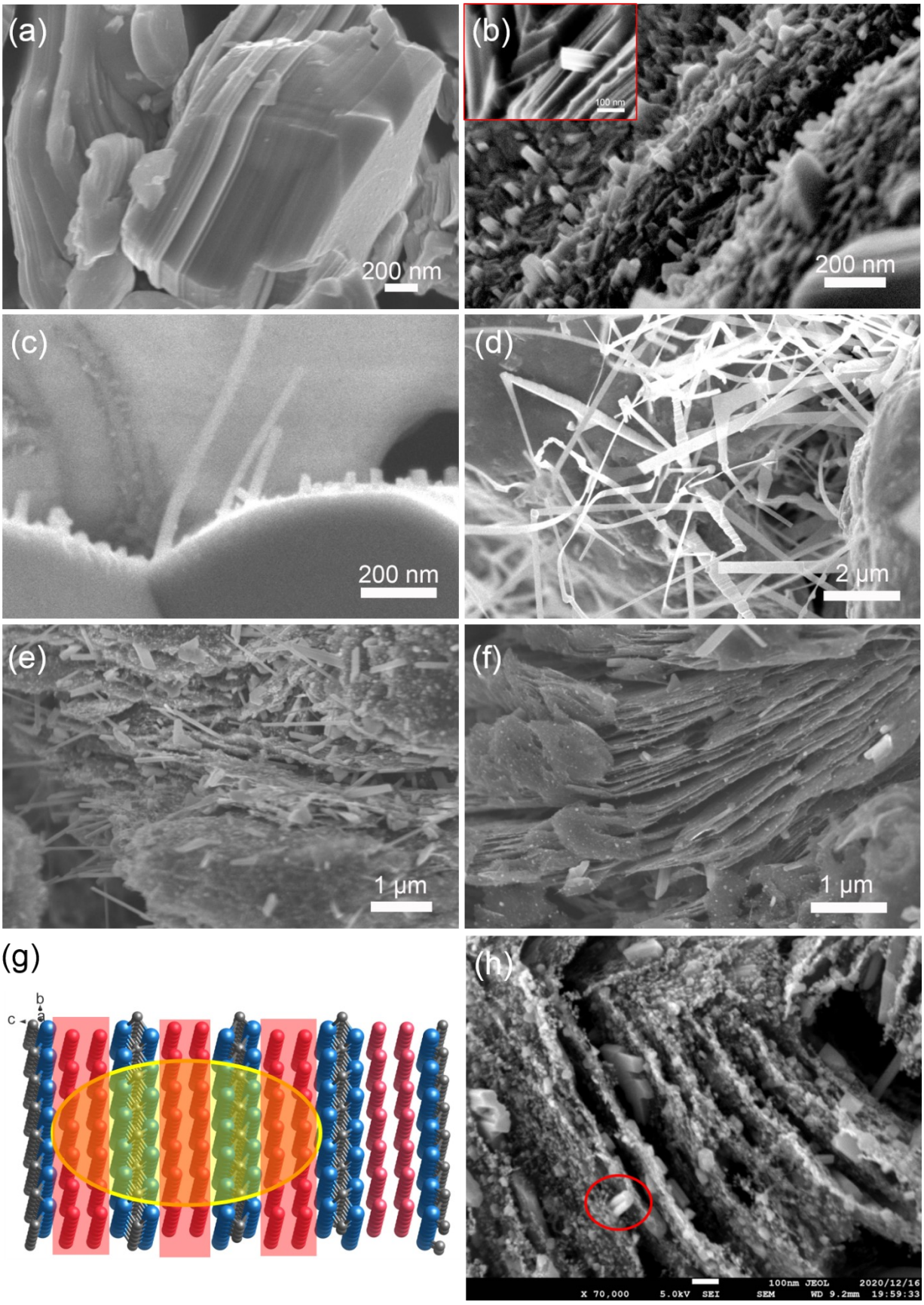

Figure S1 (a) SEM image of Mo_2Ga_2C; (b)-(f) The corresponding SEM images of the process from original

sample to nucleation, growth, and separation of 1D nanostructures. (g) Schematic diagram of dense star zone formed by the magnetic flux (Yellow circle: The dense star zone formed by magnetic field penetrating defects in graphite; Red box: magnetic field across the crystal region; Intersection area: gallium is collected in magnetic field lines). (h) The nucleus of gallium wire in Mo_2Ga_2C particles after heating in magnetic induction furnace.

As for DMT system, the template and running mechanism can be found below.

The system configuration:

The driving forces (DF): The driving force can be mainly attributed to the excitation magnetic field (H) (Figure 1f).

The assistant DF: The heating from graphite crucible and vortex current on the surface of Ga can make the Ga melting and rotating, which permit the liquid Ga to be pulled out of the MAX.

The DMT template: The DMT can be composed of some rod zones where the magnetic flux is composed of dense magnetic force lines (Figure 1f).

The running mechanism

In the flux rod zones, all the magnetic flux loss, including induction magnetic field (B) and intrinsic diamagnetic (or magnetic loss) (Figure 1f), can produce original force for drawing the Ga liquid out of the MAX. In addition, the zone can be regarded as the flux template, by which the liquid Ga can be modified into rod-like 1D structure, and be supported from flowing away by the magnetic Flux Pinning. Meanwhile, the rod-like 1D structures will grow along the DMT rod zone.

The dense star zones

Actually, the **dense star zones** can be predicted according to the structure, including defects in graphite blocks and the gaps or blank spaces in crystal microstructures. When the magnetic flux (magnetic force lines) penetrates the samples, it should be screened by the graphite block firstly (single screening effect), and then screened by MAX crystal structure successively (dual screening effect).

A) Single Screening Effect

The dynamic magnetic field itself is commonly distributed uniformly. When the magnetic lines pass through an object (graphite block, crucible, sample), some of the magnetic lines will be screened and the others can penetrate the object mostly. When the magnetic field line passes through the Al_2O_3 crucible, the dynamic magnetic field will remain uniformly distributed due to

the randomly-packed alumina particles in crucible. However, when the magnetic field lines pass through graphite block, they will penetrate the defect to form **dense star zones**, while the magnetic field lines in the rest area are screened into sparse ones.

B) Dual Screening Effect

After the magnetic force lines passing through graphite block defects, they will reach crystal Mo_2Ga_2C finally, where the screening effect by Mo_2C layer is strong, instead, that by Ga layer is weak, so that the magnetic lines across Ga layers after graphite defects have undergone dual screening effect（Fig. S1g）.

Furthermore, graphite structure defects determine the dense star zones (the yellow circle in Fig. S1g), and the crystal MGC microstructure determines the area where the Ga atoms can be collected (Fig. S1g, the red area in yellow circle) in the **dense star zone**. Due to the large defect area of the graphite block, the **dense star zone** formed by the graphite block will contain multiple Ga layers in Mo_2Ga_2C several crystal cells. Thus, the extracted Ga will be collected by DMT in the **dense star zone**, where the liquid Ga can be drawn out, merged, directed and supported by the DMT (Fig. S1h).

The **dense star zone** should be attributed to the sample structure defects, including point -, line -, and planar defects. For example, the magnetic flux pinning mechanism of maglev train, the magnetic flux line refers to the magnetic wire bundle of class Ⅱ superconductor when there is a magnetic field. The superconductor quantum flux lines are bound to the defects due to defect zone in the superconductor, which forms the **dense star zone**.

2. The Ga_2O_3 nanoribbons transported by DMT and collected by SiC substrates

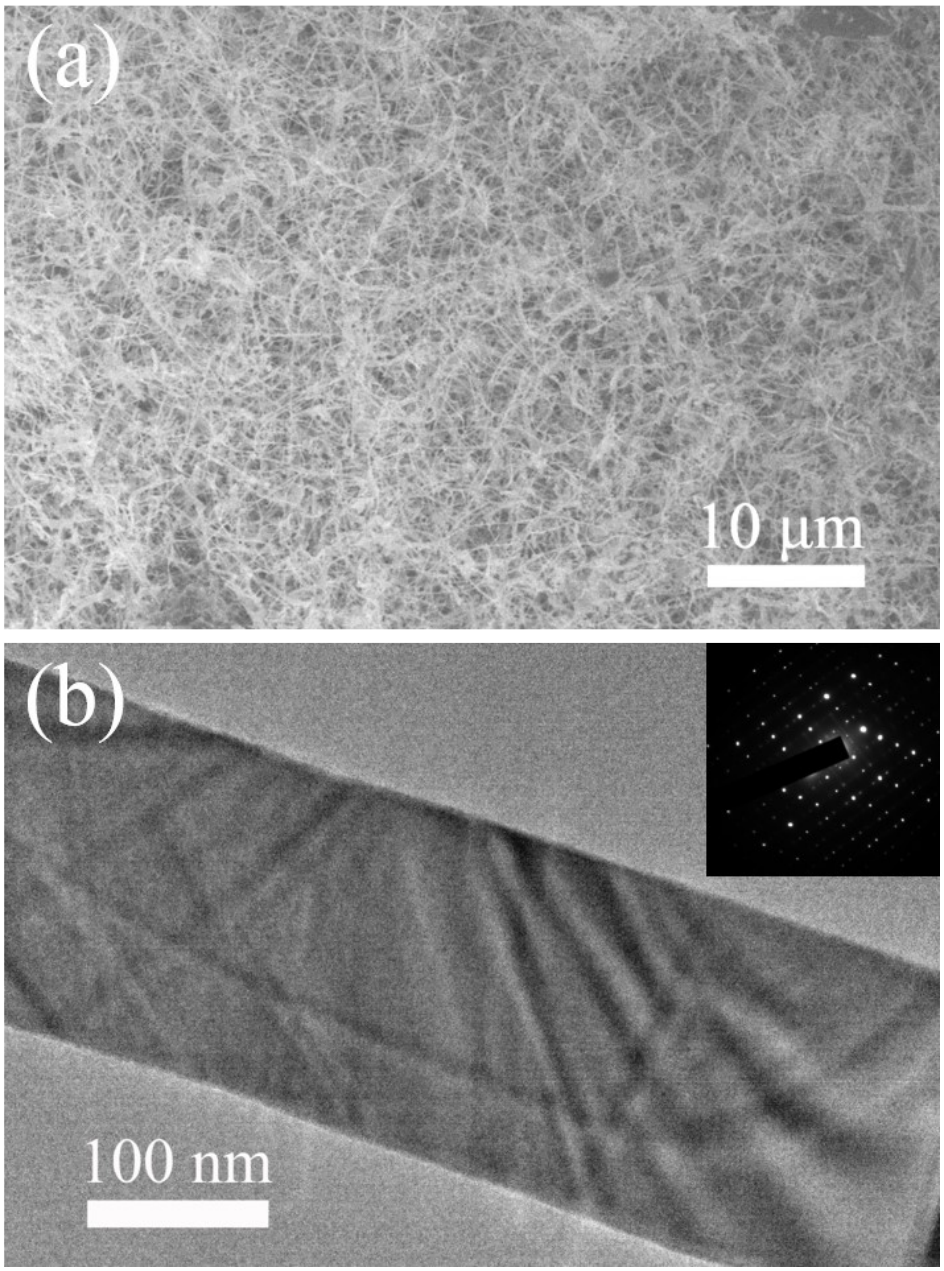

Figure S2 (a) Low-magnification FESEM image of Ga_2O_3 nanoribbons densely distributed over a large area on SiC substrate; (b) TEM image of a Ga_2O_3 nanoribbon; inset: SAED pattern.

3. The purity, structure, and valence state of Ga_2O_3 nanoribbons

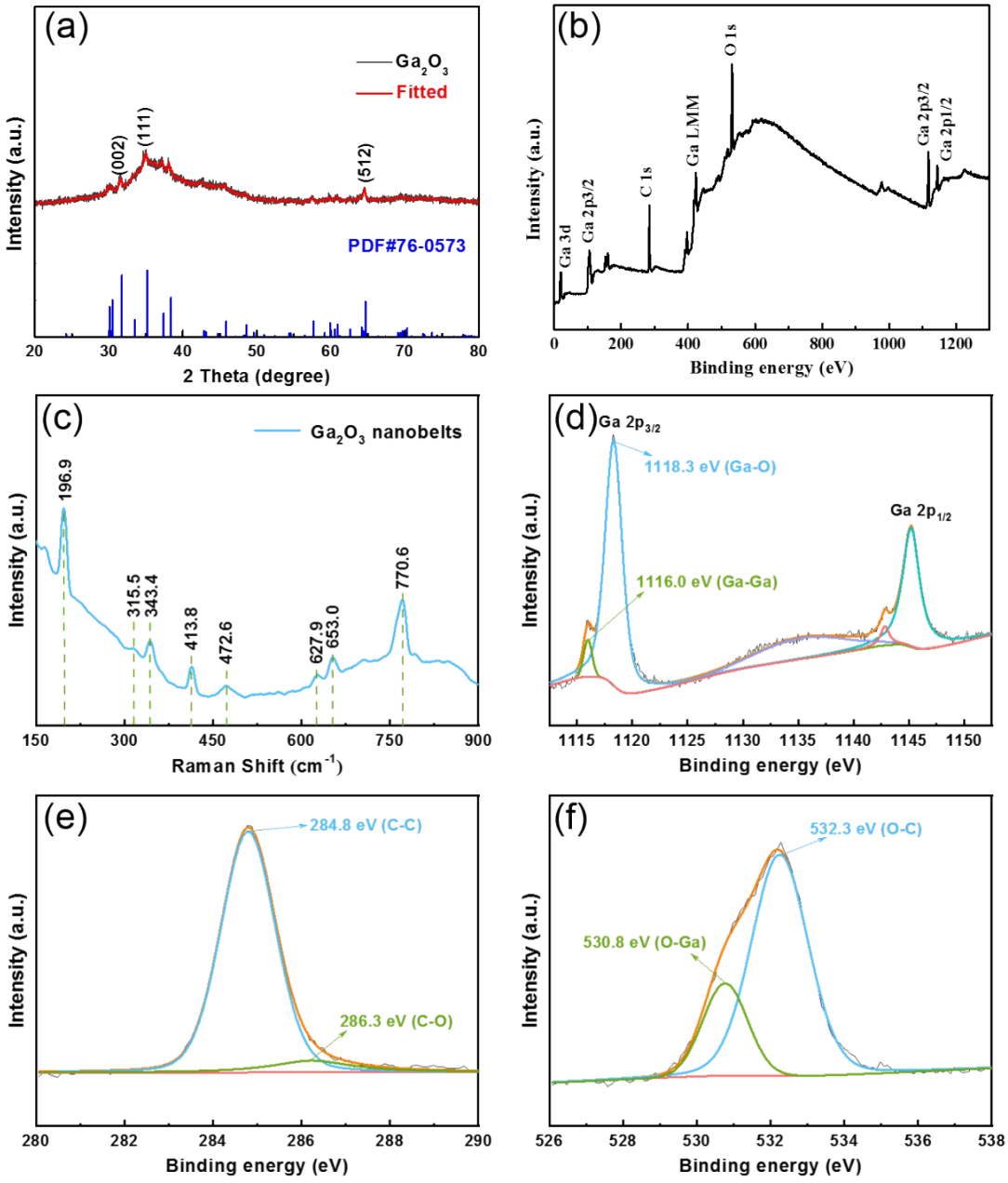

Figure S3 (a) XRD pattern of Ga_2O_3 nanoribbons; (b) XPS spectra of Ga_2O_3 nanoribbons on SiC substrate; (c) Raman scattering of the Ga_2O_3 nanobelts under 455 nm laser excitation, where all the peaks belong to the Ga_2O_3, indicating no impurity exists, and XPS spectra of (d) Ga 2p curve has been performed Lorentz fitting, and the shoulder peak represents Ga-Ga. (e) In C 1s curve, the pure C-C bonds occupy the main components and (f) the curves of O 1s can be classified into two valences.

In the XRD pattern, the characteristic diffraction peaks of the nanobelts are 31.7°, 35.2°and 64.7° (Fig. S3a), which are well-matched to the characteristic peaks of standard Ga_2O_3 cards (PDF#76-0537). The Raman spectra (Fig. S3c) show eight peaks located at 196.9, 315.5, 343.4, 413.8, 472.6, 627.9, 653.0, and 770.6 cm^{-1} respectively, which are consistent with the peaks of Ga_2O_3 in literature[1, 2]. Based on the above results, it is speculated that the nanobelts are Ga_2O_3 nanobelts. The whole XPS spectrum of Ga_2O_3 nanobelts film on SiC substrate (Fig. S3b) contains

the characteristic peaks of the Ga, C and O elements. The peaks of Ga 2p respectively correspond to Ga $2p_{1/2}$ (1142.8 and 1145.2 eV) and Ga $2p_{3/2}$ (1116.0 and 1118.3 eV) (Fig. S3d). In particular, the peaks at 1116.0 eV and 1118.3 eV should be assigned to the Ga $2p_{3/2}$ of Ga and Ga_2O_3, respectively[3, 4]. In the C1s spectrum (Fig. S3e), the strongest peak at 284.8 eV is assigned to C-C bond to the carbon as shown in EDS Mapping (Fig. 2g) surrounding or embedded in nanobelts and the peak at 286.3 eV can be attributed to C-O bond[4, 5]. As for the O 1s spectrum (Fig. 3d), the peaks are assigned to O-Ga (530.8 eV) and O-C (532.3 eV) bonds, respectively[5, 6]. No extra peaks can be found, which means just Ga, carbon and Ga_2O_3 are co-exist, without any other contamination.

4. Electrochemical measurement of the Ga_2O_3 nanobelts (Figure S4)

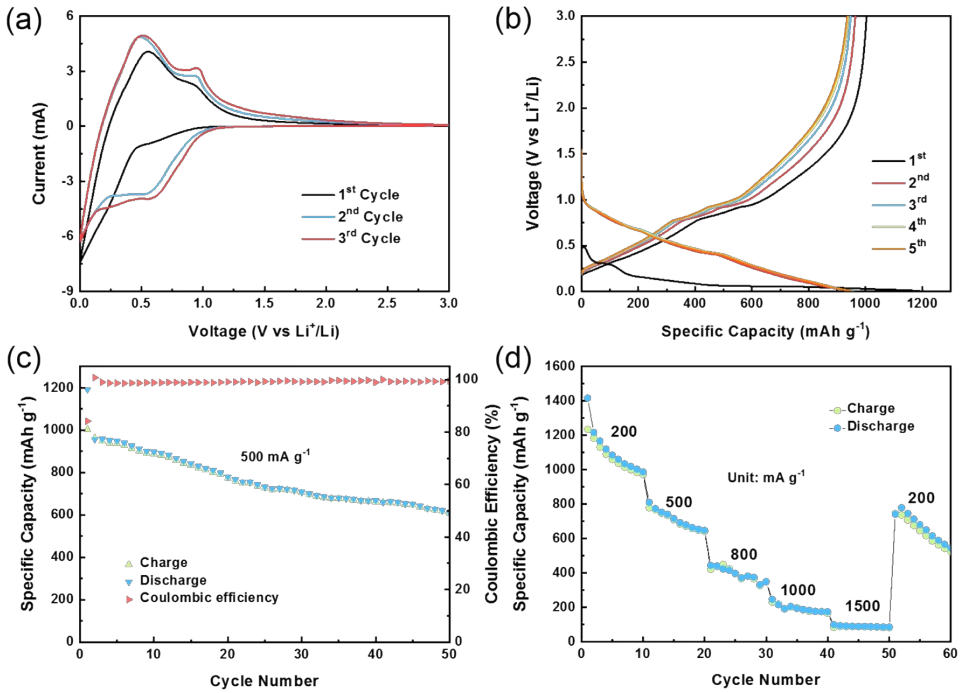

Figure S4 The initial three CV curves of the Ga_2O_3 nanobelts (0.005−3.0 V versus Li/Li$^+$, 0.5 mV s^{-1}). (b) The discharge–charge curves of Ga_2O_3 nanobelts (0.5 A·g^{-1}). (c) The cycling performance of Ga_2O_3 nanobelts (0.5 A g^{-1}, 0.005−3.0 V versus Li/Li$^+$). (d) The rate performance of Ga_2O_3 nanobelts (0.005−3.0 V versus Li/Li$^+$).

To investigate the application of Ga_2O_3 nanobelts as an anode material for LIBs, electrochemical measurements were conducted. The cyclic voltammetry (CV) test is carried out to investigate the electrochemical performance of the Ga_2O_3 nanobelts electrode with a scan rate of 0.5 mV s^{-1} from 0.005 to 3 V as depicted in Fig. S4a. The peaks of reduction and oxidation are observed at 0.55 and 0.93 V, which are considered as the lithiation of Ga to form LixGa and the delithiation of LixGa, respectively. The charge/discharge curves of the Ga_2O_3 nanobelts is investigated between 0.005 and 3.000 V versus Li/Li$^+$ at a current density of 500 mA g^{-1}. The first discharge and charge specific capacity of Ga_2O_3 nanobelts electrode are 1192 mAh g^{-1} and 1003 mAh g^{-1}. Thus, the initial Coulombic efficiency is 84%. It's worth noting that it can retain a discharge specific capacity of 948 mAh g^{-1} after 4 cycles. The Coulombic efficiencies of the subsequent cycles remain around 99% (Fig. S4b).

Cycle performance and rate performance are very important evaluation indexes for LIBs. Fig. S4c shows the cycle performance of Ga_2O_3 nanobelts electrode at a current density of 500 mA g^{-1}

for 50 cycles. After 50 cycles, the discharge specific capacity of Ga_2O_3 nanobelts electrode is 610 mAh g^{-1} and the Coulombic efficiency (CE) is approximately 99.5%. The capacity retention is 63.8% (Compared to the second discharge specific capacity of 956 mAh g^{-1}). Our results have demonstrated the best performance within 50 cycles (See table 1). The rate performance of Ga_2O_3 nanobelts electrode is investigated at current densities from 200 to 1500 mA $g^{-1}$and back to 200 mA g^{-1} (Fig. S4d). The average discharge specific capacities of Ga_2O_3 nanobelts at current densities of 200, 500, 800, 1000, 1500 and 200 mA g^{-1} are 1111, 713, 395, 212, 99 and 617 mAh g^{-1}, respectively.

Table S1. The summarization of cycling performance of various Ga_2O_3-based electrodes.

Electrode	Current density/mA g^{-1}	Capacity/mAh g^{-1} (Cycle number)	Ref.
Ga_2O_3 nanobelts	500	~610 (50)	This work
β-Ga_2O_3	50	~263 (40)	[14]
Ga_2O_3-rGO	50	~770 (40)	[14]
β-Ga_2O_3 nanorods	400	~330 (30)	[15]
3D Ga_2O_3/C	500	~270 (50)	[16]
Ga_2O_3/NC NPs	200	~560 (50)	[17]

5. DMT application towards Al element (Figure S (5-10))

The DMT method should be applicable to metal materials with higher melting points. Here, the

Ti_3AlC_2 was selected as the raw material for aluminum 1D structures. The sample collected on graphite paper is shown in Figure S5a. It can be observed that the film was formed by stacking nanorods into piles which were wide at the bottom and narrow at the top. Moreover, the sizes of nanorods are in a factor of magnitude of hundred nanometers, meanwhile, the lengths can reach to over ten microns. The large area uniform distribution of nanorods can be observed (Figure S5b), suggesting the nanorods structures can be fabricated on a large scale. The sample collected on SiC substrate is shown in Figure S5c-d. The cross-section sizes of rods look uniform around 100-200 nm (Figure S6a). Figure S6b illustrates that the nanorod owns a crystal structure, where the lattice-interspacing between the adjacent crystal planes can be calculated. The crystal axis [020] conforms the characteristic of Al_2OC. In addition, the inset indicates the nanorods are well-organized monocrystalline structure (Figure S6b), since only a set of regular diffraction spots are observed. Figure S6c is the cross-correlation of the region marked by the yellow box in Figure S6b, showing an atomic lattice of (020) crystal plane, which is consistent with the simulation results (Figure S7). Figure S6d-g are the corresponding EDS Mapping of the nanorod, exhibiting the uniform distribution of Al, O, and C elements. A carbon film coating on the nanorod have been found, which can be proved by the sample soaked in hydrochloric acid (Figure S8a). Combined with EDS, it can be inferred that this film is a carbon film. the Raman spectra (Figure S8b) of the samples collected on SiC substrate showed three peaks at D, G and 2D, respectively, which further confirmed the existence of the outer carbon film of the nanorods [7].

Figure S9a is the XRD pattern of the product prepared with Ti_3AlC_2 as raw material and the peaks located at 33.5°, 35.5°, 48.8°, 58.0° and 69.8° are consistent with PDF#36-0148, indicating that the main component of the sample is Al_2OC [8], and another peak at 43.4° can be attributed to Al_2O_3. The entire XPS spectrum scanning contains the characteristic peaks of Al, C, and O elements (Figure S10). The Al 2p spectrum, splitting into two peaks with Lorentz fitting (Figure S9b). The binding energies of 73.5 eV and 74.9 eV are assigned to Al-C and Al-O bonds, respectively. The peak in the C 1s spectrum (Figure S9c) is trimodal, and the binding energies of the corresponding three single peaks are 284.6 eV, 285.5 eV and 288.9 eV, which are assigned to C-C, C-Al and C=O bonds respectively. The C-C bond peak at 286.4 eV may come from the carbon film epitaxial spreading on the surface. In the O 1s spectrum (Figure S9d), the peak at 532.5 eV is attributed to O-Al bond [8].

The formation process of Al_2OC nanorods is similar that of Ga_2O_3 nanobelts mentioned above. The Al rod nucleates first, and then reacts with carbon oxide to ge10nerate Al_2O_3 and Al_2OC [9], and successively the Al_2OC can transferred to Al_2O_3 proportionally [8]. Meanwhile, the released carbon from the redox process forms graphene on the rod surface (See Figure S8).

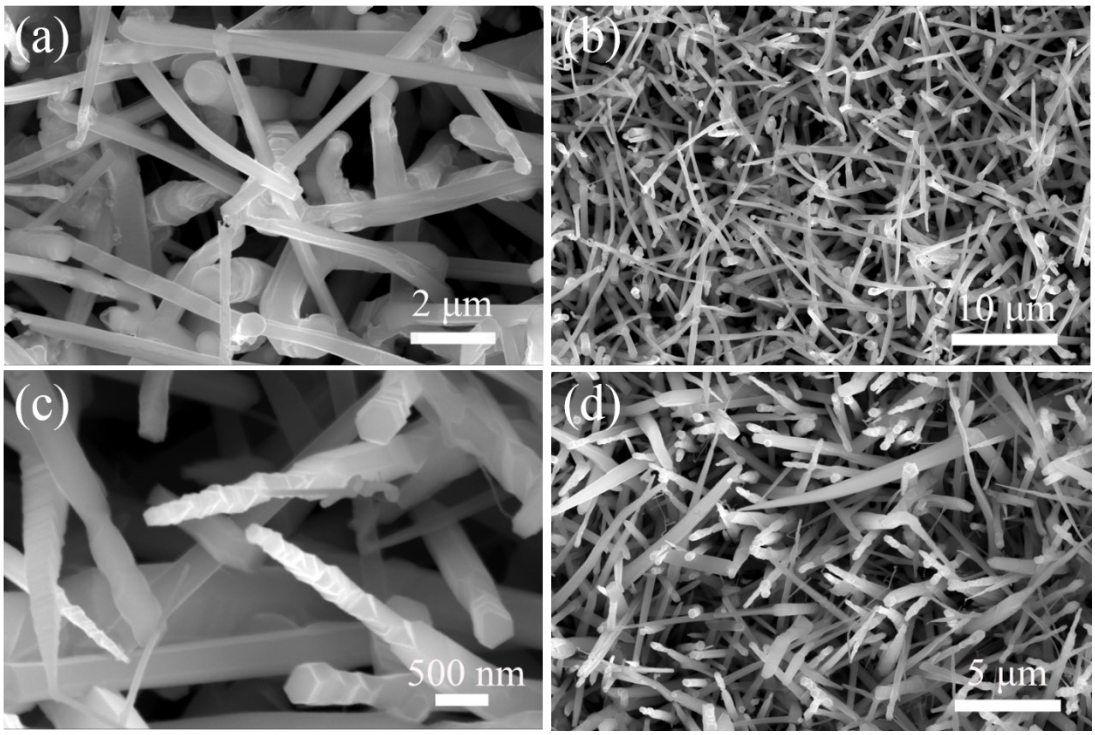

Figure S5 (a) High-magnification FESEM image of Al_2OC nanorods collected on graphite paper; (b) Low-magnification FESEM image of Al_2OC nanorods collected on graphite paper; (c) High -magnification FESEM image of Al_2OC nanorods collected on SiC substrate; (d) Low-magnification FESEM image of Al_2OC nanorods collected on SiC substrate.

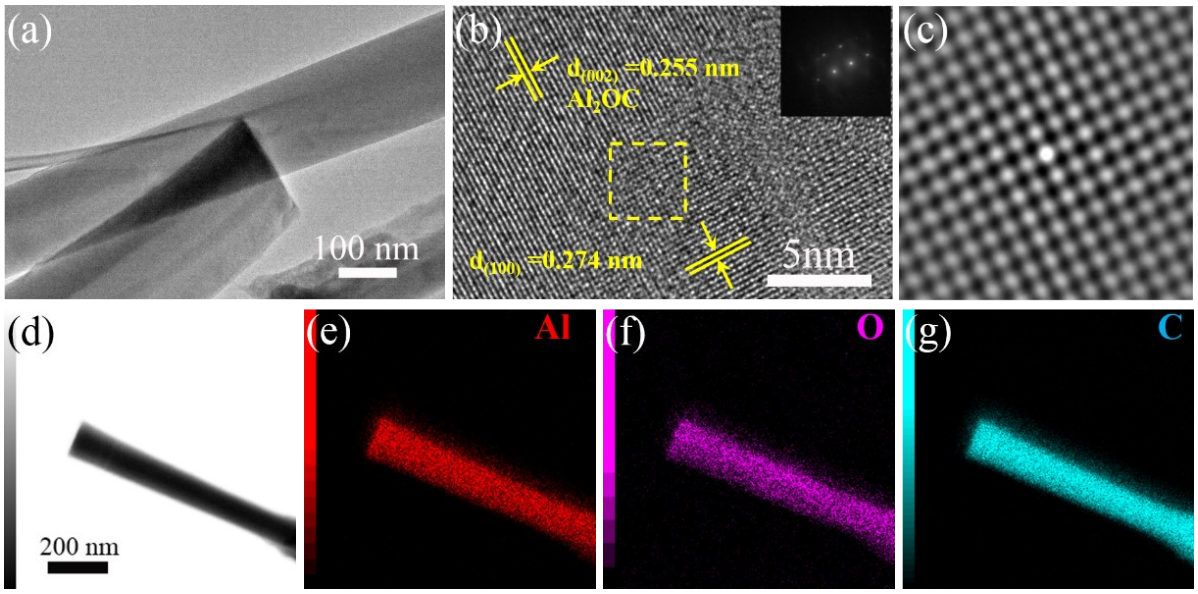

Figure S6 Morphologies and components of Al_2OC nanorods collected on graphite paper. (a) Al_2OC nanorods are uniform in size. (b) Lattice fringe shows view direction is along [010], inset: SAED pattern; (c) The cross-correlation of the region marked by the yellow dotted box in (b); (d) TEM image; (e)–(g) Al, O, and C elemental mappings of the Al_2OC nanorod.

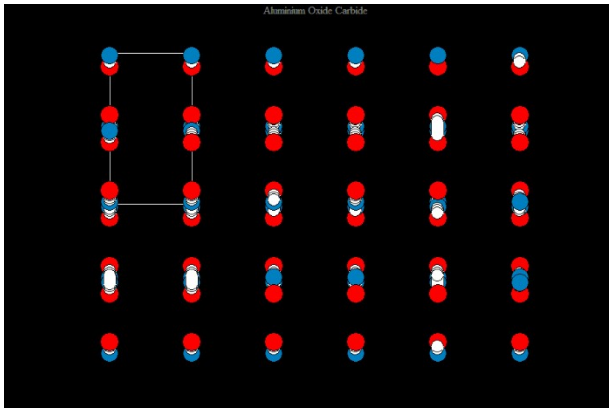

Figure S7 Simulation of atom distribution on (020) crystal plane of Al_2OC.

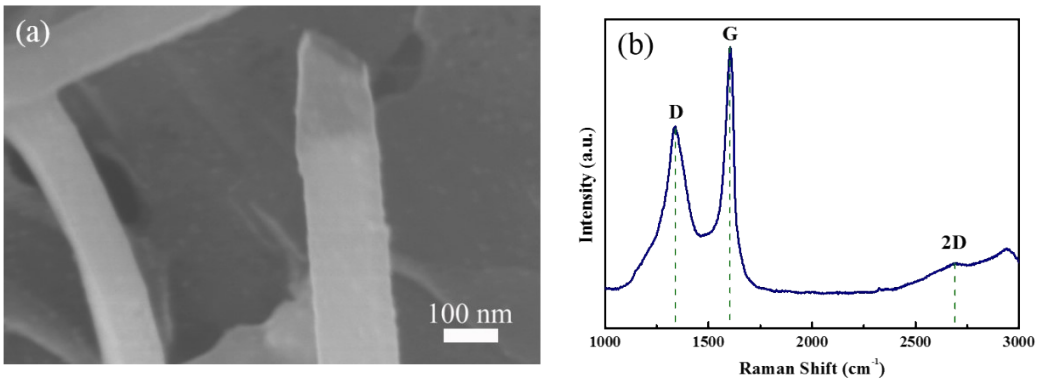

Figure S8 (a) FESEM image of Al_2OC nanorods corroded by hydrochloric acid; (b) Raman scattering of Al_2OC nanorods on SiC substrate corroded by hydrochloric acid from 1000 to 3000 cm^{-1}.

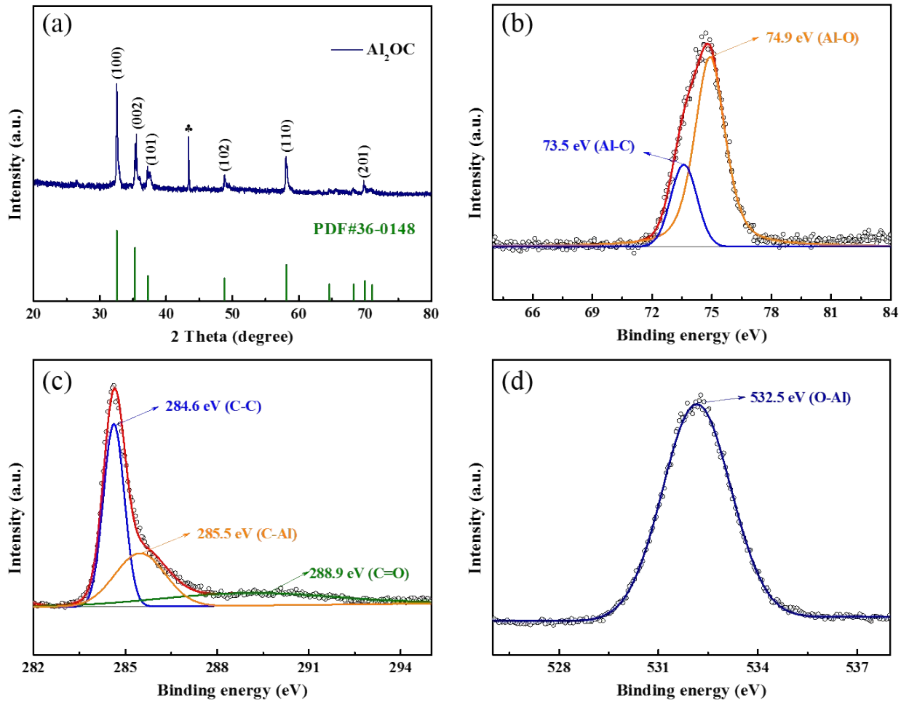

Figure S9 XRD pattern and XPS spectra of Al_2OC nanorods. (a) XRD pattern, only one impurity peak was found, marking by black plum blossom. XPS spectra of (b) Al 2p, (c) C 1s, Lorentz fitting illustrating the pure C-C occupy the dominant. (d) O 1s.

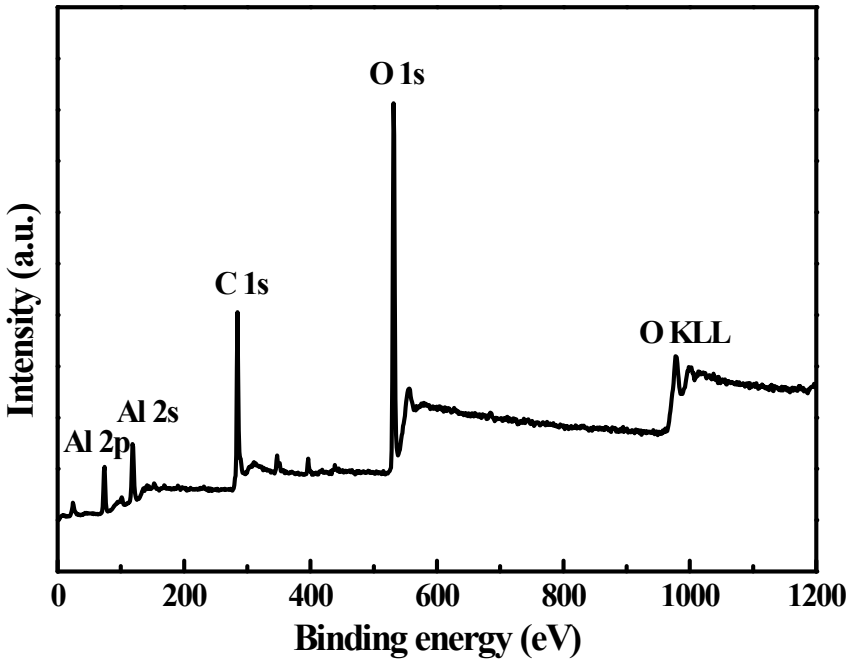

Figure S10 XPS spectra of Al_2OC nanorods.

6. DMT application towards Si element (Figure S (11-21))

A MAX phase with non-metallic element (Si) in the A-layer has been presented to demonstrate the formation process of silicon nanowires (SiNWs). The dense SiNWs has been collected by SiC substrate (Fig. S11a). The diameter size of the SiNWs was evaluated from more than 200 nanowires (Fig. S11b), by which the diameter of the nanowires can be estimated in around 30-50 nm, and the length can be adjusted by changing some specific parameters (Fig. S12). The sample collected on the graphite paper (Fig. S13a-b) demonstrated the same morphological characteristics as that on SiC substrate. The nanowires which have a stacked structure gradually became longer and thinner without bamboo-like structure, suggesting a DMT bear the nanowire's weight, instead of the VS mechanism[10]. TEM was employed to further investigate the morphology of an individual SiNWs (Fig. 14a), exhibiting an accordion-like layered structure, and we can find the gaps between layers are obviously. The same structural features are a typical characteristic for the SiNWs (Fig. S15). The accordion-like does not guarantee the gap is the real interspacing in the lattice (Fig. S14b), and the SAED as inset indicates that the synthesized SiNWs had a single crystal structure. The Delta-lattice structure can be found in Fig. S14c, which obtained by cross-correlation processing of the region marked by the yellow box in Fig. S14b. This lattice layout indicates the SiNWs have a high-quality crystal structure. When we check the nanowire along diameter direction, a densely-stacked plane (111) can be observed (Fig. S14c), in consistent with the simulation (Fig. S16). Thus, the plane stacking along the axis is (110) series plane. The corresponding EDS Mappings (Fig. S14d-g) show the distribution of Si, O and C elements. To further confirm the distribution of elements on the nanowires, Si, O, and C elemental line-scan profiles were employed. As shown in Fig. S17, the crystalline silicon nanowire is surrounded by carbon. Due to the presence of oxygen and carbon oxide, we also observed SiNWs with the same layered structure but surrounded by an amorphous oxide shell, and its TEM and EDS Mappings are shown in Fig. S15b and S18a-d. For the nanowires with spheres at the top or middle, we also performed TEM images and EDS Mappings characterization (Fig. S15d and S18e-h). The Si, O, and C elemental line-scan profiles (Fig. S17b-d) of this kind nanowires further demonstrate that there is an amorphous oxide shell surrounding the nanowires. The silicon in the backbone can be observed to be twisted, and the outside are also surrounded by an amorphous oxide shell. Fig. S19 shows a process state of the formation of the head sphere. The wire also maintains a layered

structure, and the sample is analyzed in the support material.

The X-ray diffraction (XRD) characterization of the SiNWs collected with SiC substrate and SiC substrate is shown in Fig. S20a. Except for the peaks of SiC substrate, the rest of the peaks located at 28.3°, 35.5°, 47.2°, 56.1°, 69.1°, 76.2°, and 87.9° belong to the SiNWs. These peaks can be fully indexed as the (111), (220), (311), (400), (331) and (422) planes of crystalline silicon (PDF#27-1402), which is consistent with the literature[11]. The XRD pattern of SiNWs collected on graphite paper (Fig. S21) exhibits the same result with that on SiC substrate. Raman spectrum provides further structural information (Fig. S20b). The peaks of the 1D nanowire on graphite paper are same with the sample on SiC substrate. Their peaks located at 518.2 and 964.6 cm^{-1}, corresponding to the first-order transverse optical phonon mode (TO) and second-order transverse optical phonon mode (2TO) of silicon [12, 13], respectively. In addition, the peak at 518.2cm^{-1} is wider and asymmetric compared to the previously reported single silicon crystal, with a slight blue shift, which is the typical characteristic of silicon nanowires coated with amorphous silicon oxide. The SiNWs film on SiC substrate can screen the peaks of the substrate, indicating the film is thick enough to cover the substrate.

The above results confirmed that the 1D nanomaterials is SiNWs surrounded by amorphous silica.

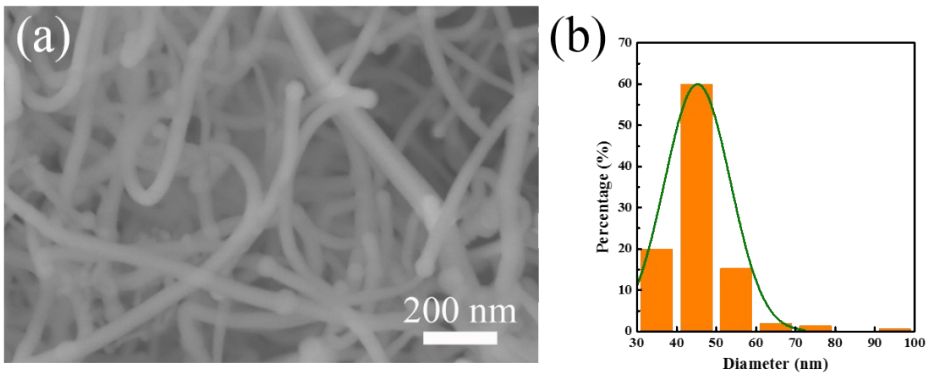

Figure S11 Characterization of SiNWs collected on SiC substrate: (a) FESEM image; (b) Diameter distributions of the SiNWs from SEM analysis.

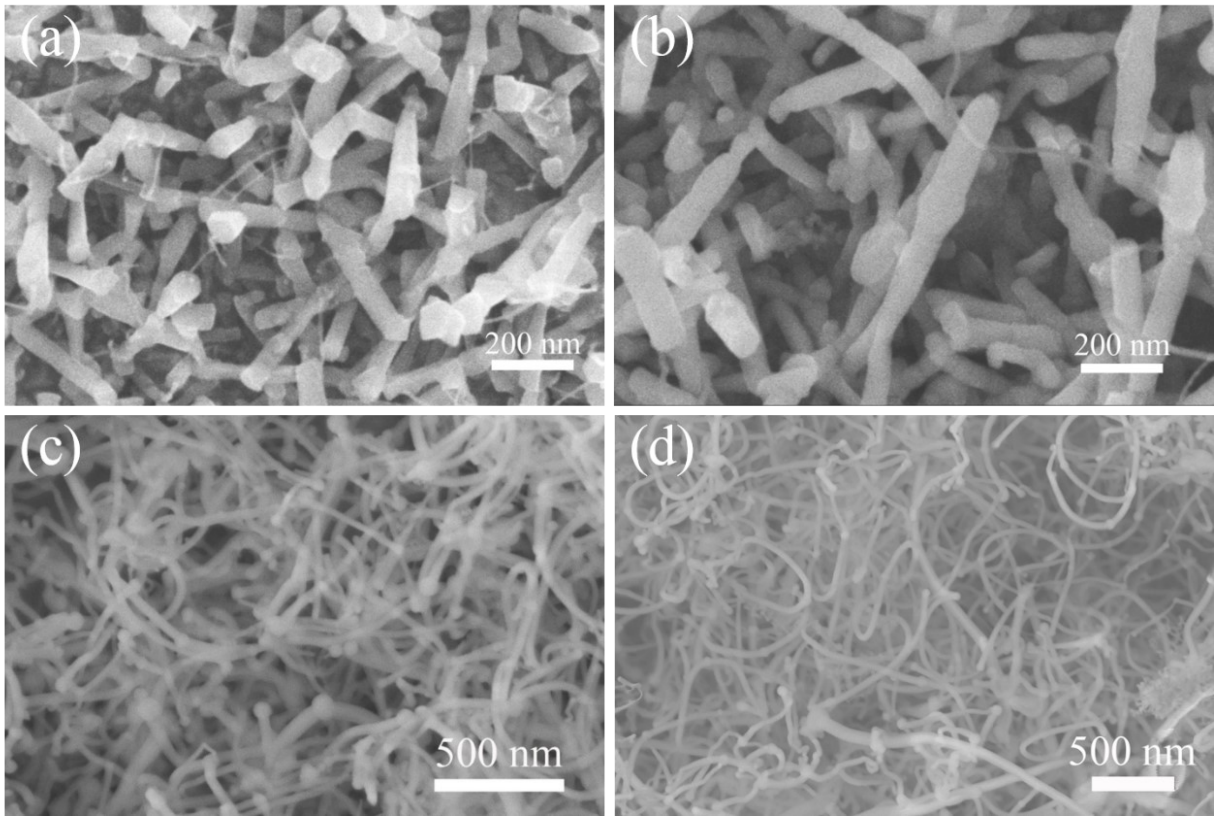

Figure S12 FESEM image of SiNWs prepared with different amounts of Ti_3SiC_2 on SiC substrate: (a) 32 mg; (b) 64 mg; (c) 96 mg; (d) 128 mg.

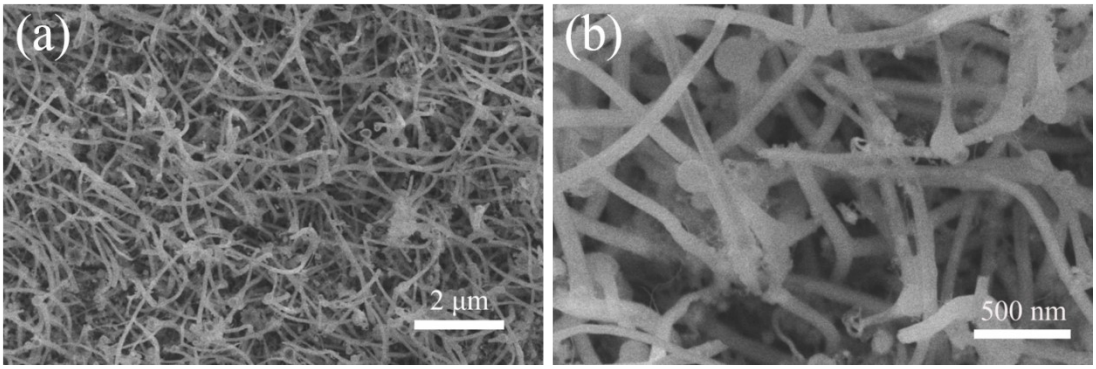

Figure S13 (a) Low-magnification FESEM image of SiNWs collected on graphite paper; (b) High-magnification FESEM image of SiNWs collected on graphite paper.

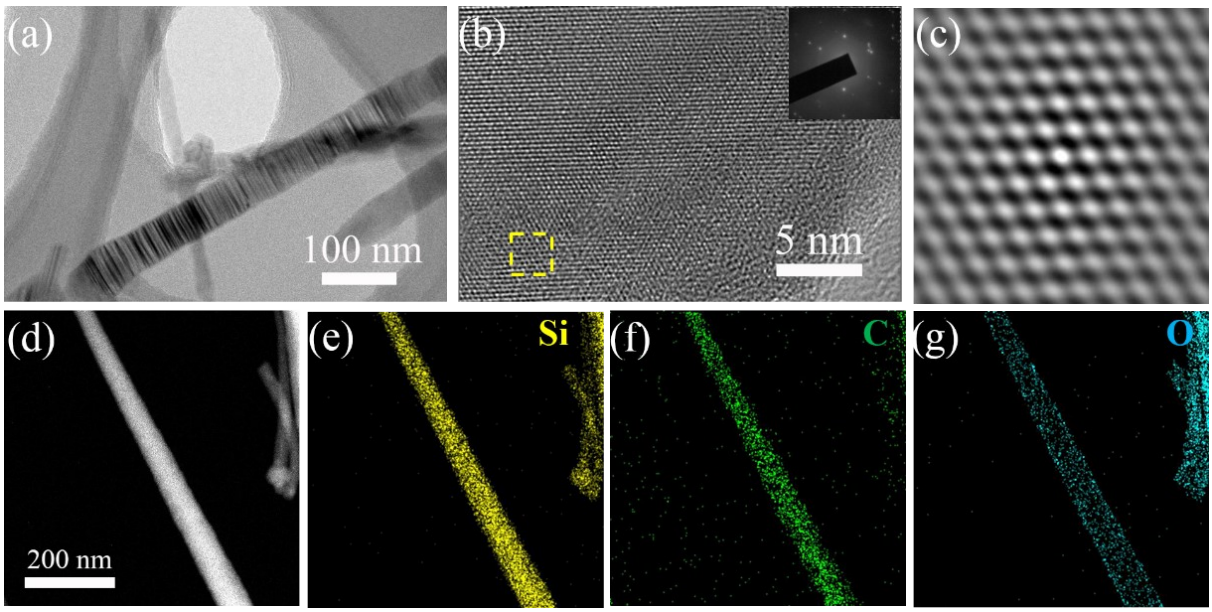

Figure S14 Morphologies and components of SiNWs on SiC. (a) SiNWs collected on SiC substrate; (b) SiNWs on SiC, viewing along [111] direction, inset: SAED pattern; (c) The cross-correlation of the region marked by the yellow dotted box in (b). (d) TEM image; (e)–(g) Si, O, and C elemental mappings of the SiNW collected on SiC substrate.

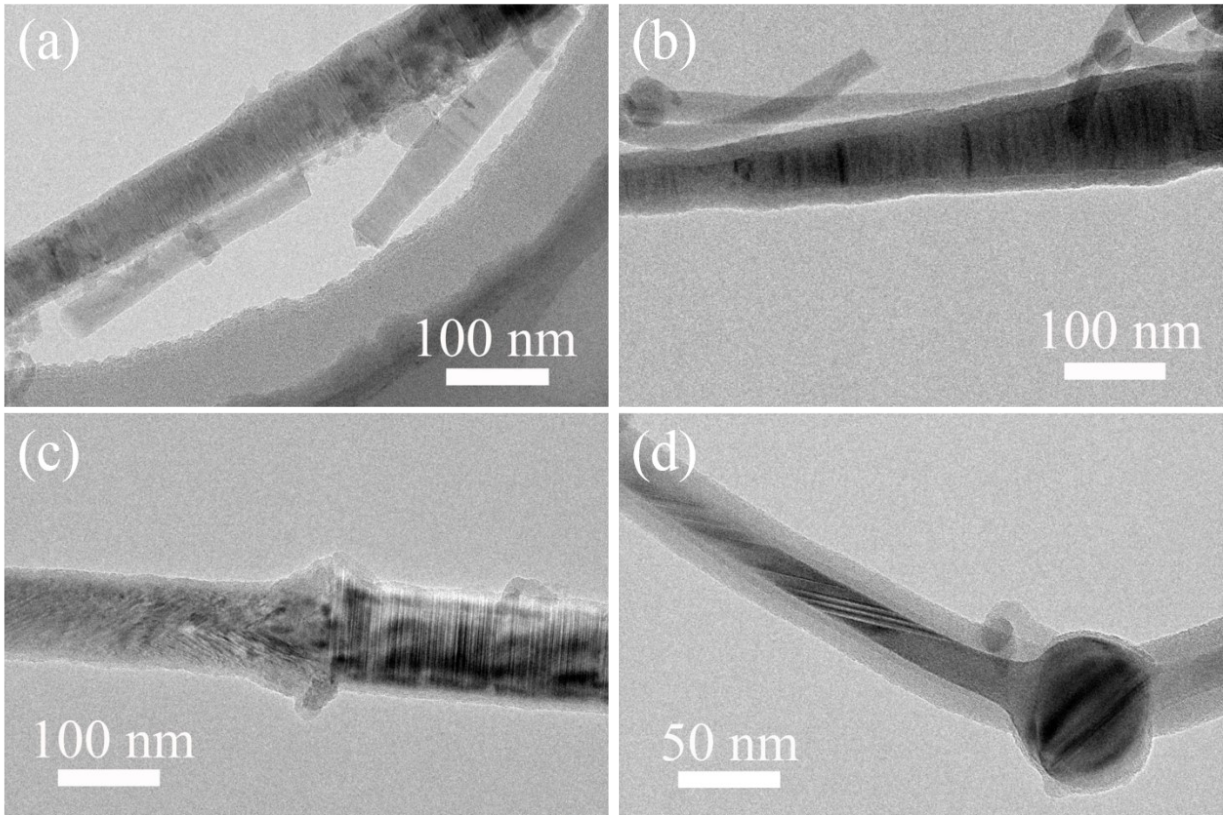

Figure S15 TEM image of SiNWs: (a)-(c) SiNWs with the same layered structure but surrounded by an amorphous shell; (d) a SiNW with a sphere and surrounded by an amorphous shell.

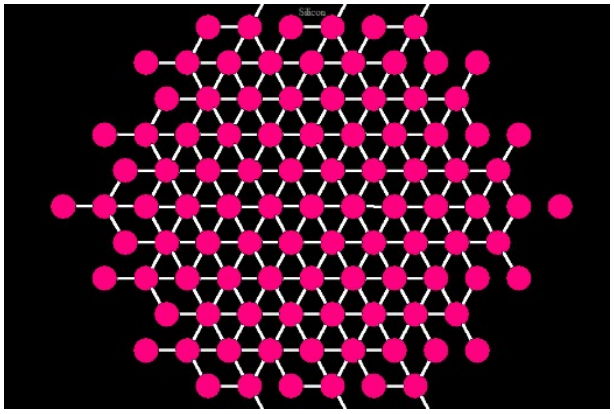

Figure S16 Simulation of atom distribution on (111) crystal plane of Si.

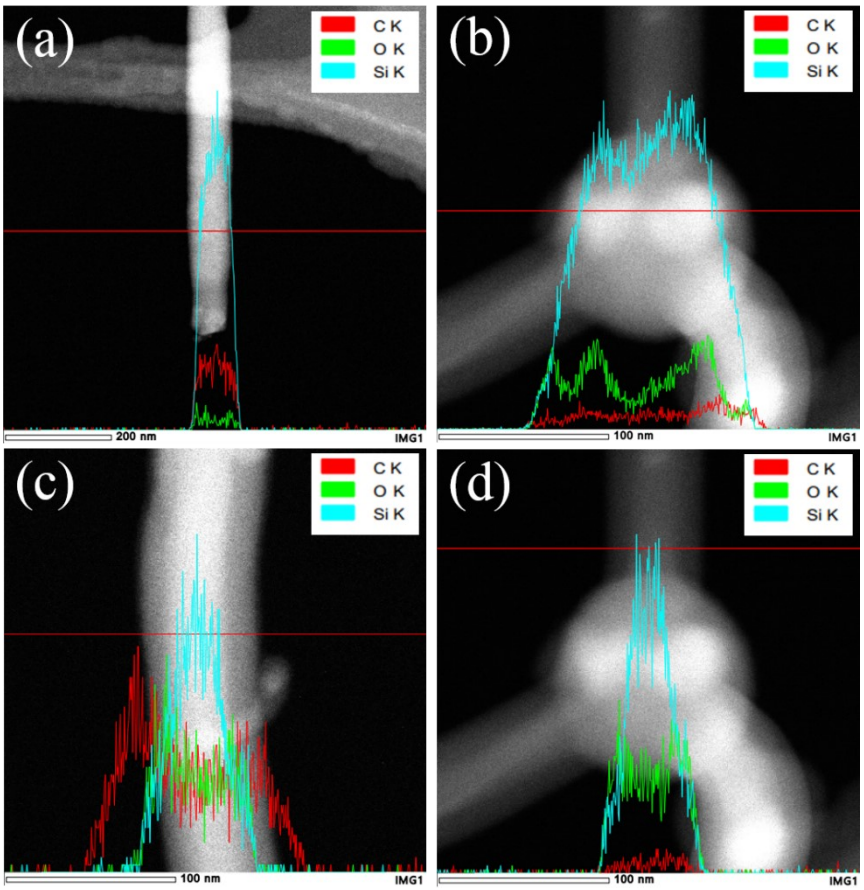

Figure S17 (a) TEM image and Si, O, and C elemental profiles of SiNW without sphere and amorphous shell; (b)-(d) TEM image and Si, O, and C elemental profiles of a SiNW with a sphere.

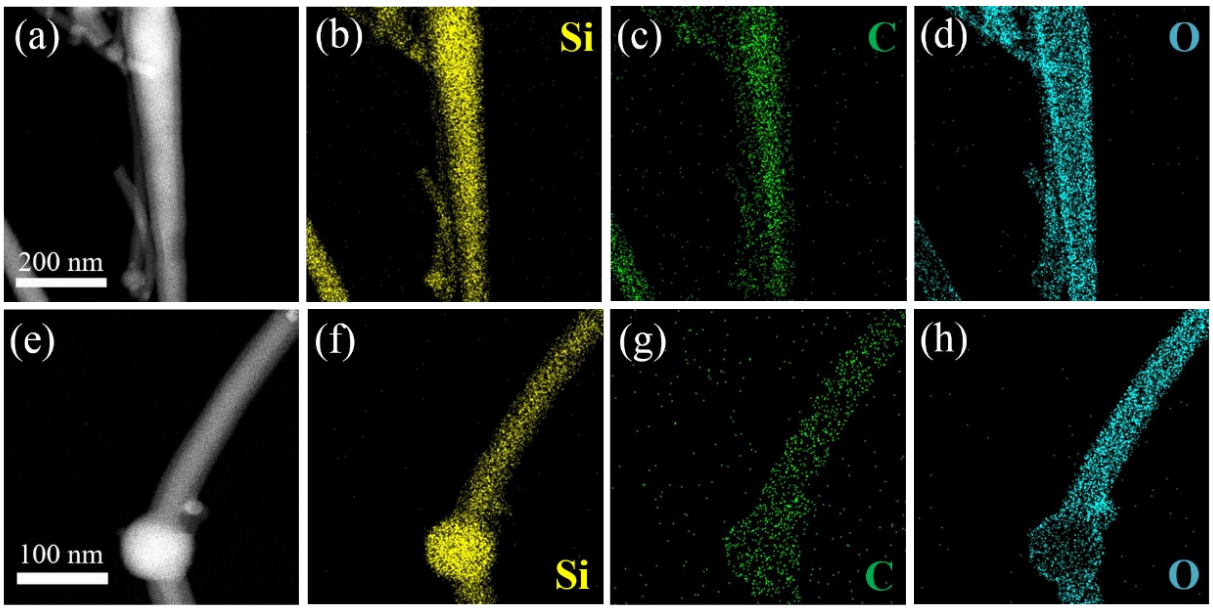

Figure S18 (a)-(d) TEM image and Si, O, and C elemental mappings of an individual SiNW with the layered structure and surrounded by an amorphous shell; (e)-(h)TEM image and Si, O, and C elemental mappings of an individual SiNW with a sphere and surrounded by an amorphous shell.

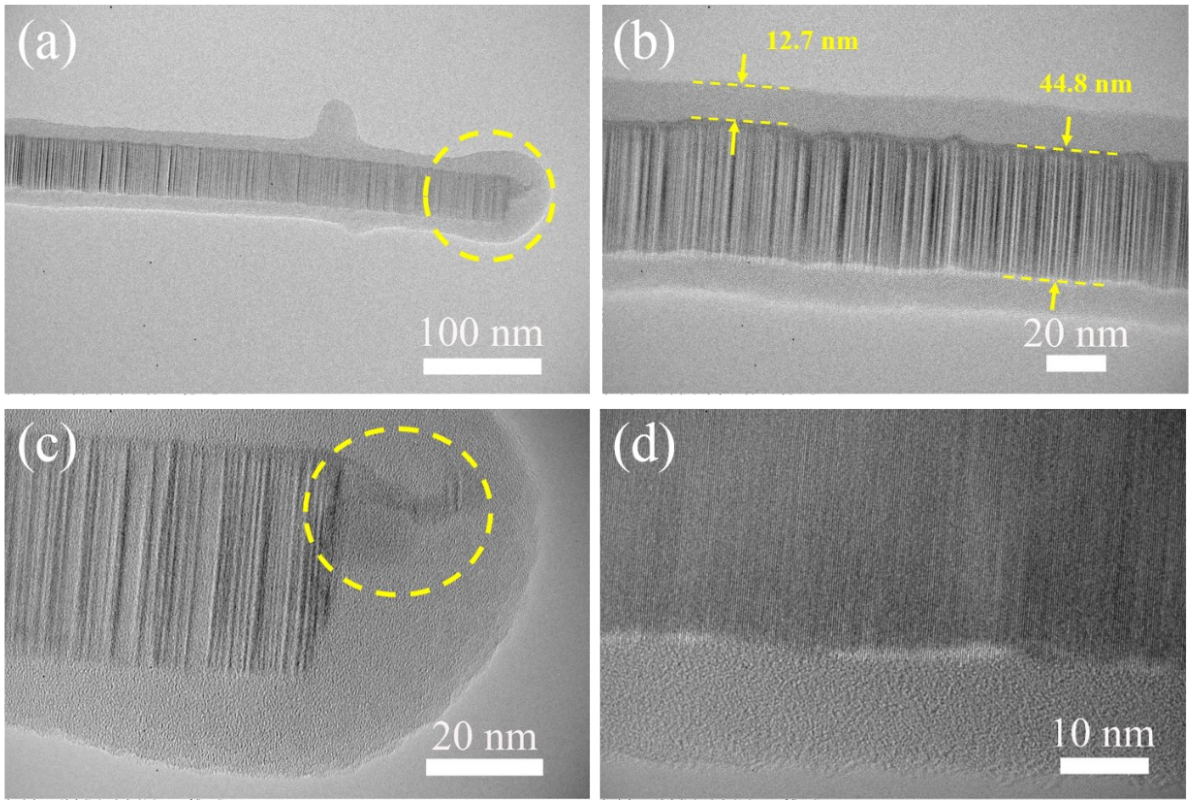

Figure S19 TEM image of an individual SiNW with the layered structure and surrounded by an amorphous shell.

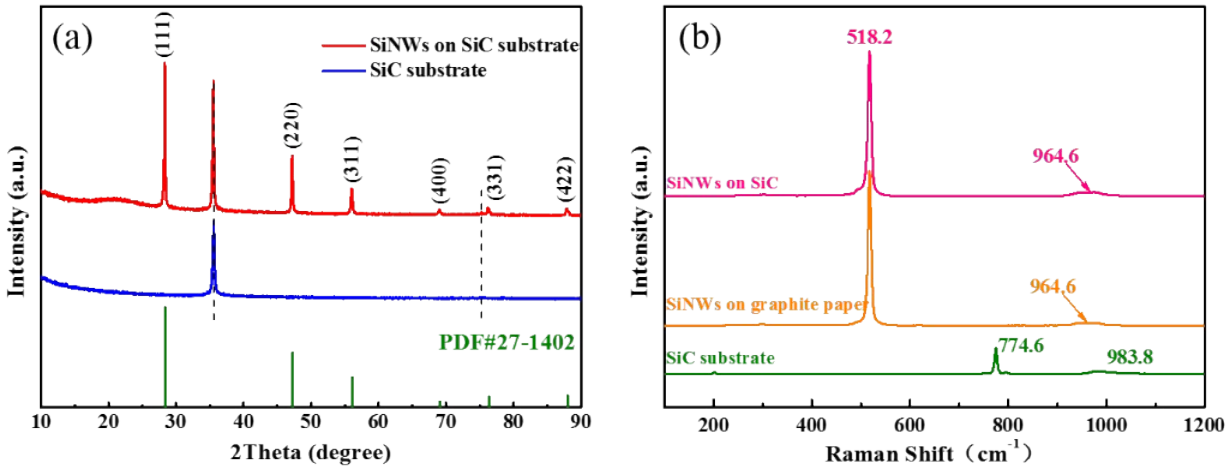

Figure S20 SiNW structure and components. (a) XRD pattern of SiC substrate and SiNWs collected on SiC substrate, where no impurity is found. (b) Raman scattering of the SiC substrate (Green curves), and the SiNWs on SiC substrate (Red cures) and the SiNWs on graphite paper (Yellow curves) under 455 nm laser excitation, implying the silicon peaks are well-defined.

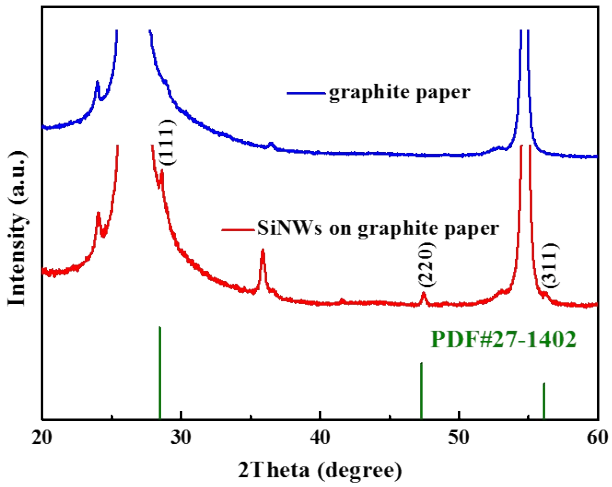

Figure S21. XRD pattern of graphite paper and SiNWs collected on graphite paper.

The growth mechanism

In the main text, we have discussed the formation and nucleation mechanism of element 1D materials via DMT. Here we further discuss the growth mechanism to 1D silicon nanowires. Firstly, the "A" element in the MAX (Ti_3SiC_2) crystal structure can be collected into liquid nuclei and pulled out of the substrate under Dual Screening Effect. When the liquid nucleus formation, it was forced into spinning state around the liquid axis by the vortex current from induced current (See Figure 1f rotation mode). The liquid nucleus continues to elongate and grow along the direction of magnetic flux. With growth proceeding, the liquid silicon away from the MAX substrate become cooling and solidifying into silicon nanowire (Fig. S19a). Depending on the growth atmosphere, the solid silicon nanowires can become oxidized in the surface layer (Fig. S19b). When the silicon layer in MAX was exhausted, the nanowire continues pinned and directed to collecting substrate by DMT. When nanowires fly away from the MAX to the collecting substrate, they are quenched because of the substrate temperature is much lower than that in MAX. The layered structure can be observed clearly, suggesting the spinning state can be kept by quenching (Fig. S19b). In addition, as for the element Ga and Al, they almost underwent a growth process following the same mechanism if keeping vacuum good enough.

7. **The nitrogen in 1D structure based on the Al element might come from MAX only (Figure S22-23)**

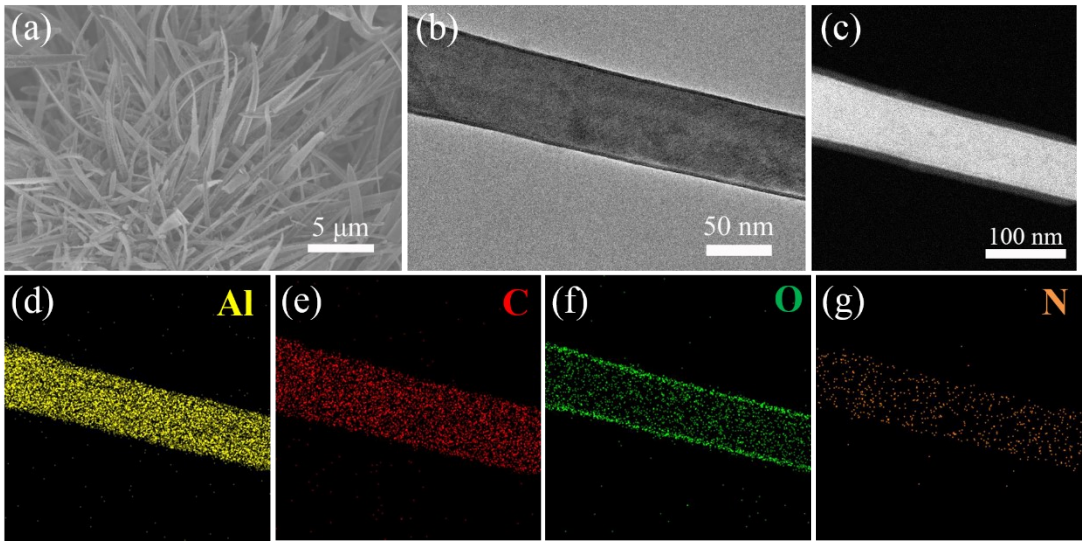

Figure S22 Characterization of nanorods prepared from Ti_3AlN_2 on graphite paper: (a) FESEM image; (b) and (c)TEM image; (d)–(g) Al, C, O, and N elemental mappings of the nanorod.

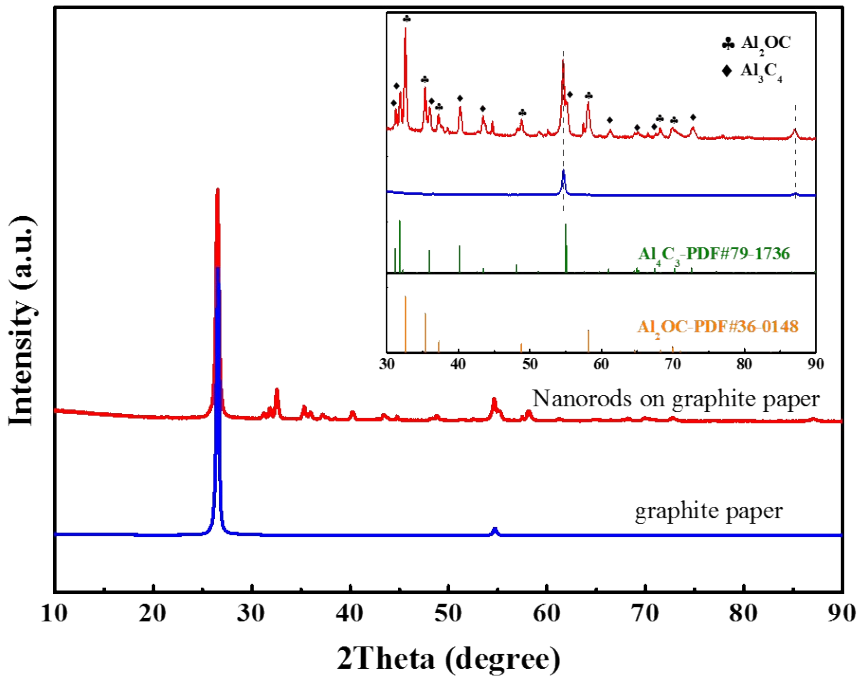

Figure S23 XRD pattern of graphite paper and the nanorods prepared from Ti_3AlN_2 on graphite paper; inset: partial enlargement from 30° to 90°.

To investigate the source of the carbon that coats of 1D nanomaterials, we used Ti_3AlN_2 as the raw material to prepare 1D nanomaterials with the magnetic excitation method. The SEM (Figure S22a) and TEM images (Figure S22b) show the 1D nanostructure of the sample. And the Al, C, O, and N elemental mappings (Figure S22c-g) of the nanorod indicate that the carbon comes from the graphite block and the nitrogen comes from Ti_3AlN_2. XRD pattern (Figure S23) of graphite paper and the 1D nanomaterials prepared from Ti_3AlN_2 on graphite paper further demonstrate that the main components of the samples are Al_2OC and Al_3C_4 corresponding PDF#36-0148 and PDF#79-1736, respectively. These results indicate that the outer carbon coating of 1D nanomaterials may come from graphite blocks or MAX phase, where graphite blocks may be the main source.

Materials and Methods

Preparation of one-dimensional nanomaterials. We use the new ternary layered ceramic material MAX (The general chemical formula is $M_{n+1}AX_n$, where M is a former transition metal, A is mainly group IIIA and IVA elements, X is carbon and/or nitrogen, n=1~3) as the raw material for the preparation of one-dimensional nanomaterials, and specifically select three representative materials of A elements: Mo_2Ga_2C, Ti_3AlC_2, and Ti_3SiC_2. The specific experimental steps are: First, weigh 64 mg MAX raw material and spread it on a graphite block with circular grooves at the four corners (the length, width, and height of the graphite block are 17 mm, 17 mm and 10 mm, respectively, and the diameter and depth of the circular groove are respectively ~3 mm and ~6 mm) (step 1). Place the graphite block flat in the alumina crucible, and then cover the graphite block with graphite paper, SiC substrate or carbon fiber cloth to ensure that the four grooves can be completely covered and close to the graphite block (step 2). Then place the alumina crucible in the magnetic induction furnace, and keep the graphite block level during the placing process, that is, ensure that it is parallel to the coil (step 3). The three raw materials are heated by magnetic induction at different powers for different times under the protection of 10 kPa argon gas (step 4), and finally the corresponding 1D nanomaterial film is collected on the graphite paper, SiC substrate or carbon fiber cloth (step 5). The specific parameters are: Mo_2Ga_2C is heated by magnetic induction at 25.4 kW for 48 s, Ti_3AlC_2 is heated at 28.5 kW for 88 s, and Ti_3SiC_2 is heated at 29.4 kW for 43 s.

Measurements. The morphology of the collected samples on the graphite paper or SiC wafer substrate was characterized by field emission scanning electron microscope (FEI SEM, JSM-7610F, JEOL Ltd., Japan). Specimens for transmission electron microscopy (TEM) investigation were prepared by dispersing 1D nanomaterials on a copper mesh after dilution in methanol and ultrasonication. High-resolution transmission electron microscope (HRTEM, JEM-F200, JEOL Ltd., Japan) was used to characterize the surface and lattice details of a single 1D nanomaterial under an accelerating voltage of 200 kV. Use energy dispersive x-ray (EDX) to characterize the elemental composition of the material. To further determine the composition of the sample, the X-ray diffraction (XRD) pattern of the sample was recorded on an EMPYREAN with Cu Kα rays (λ = 1.5406 Å). Raman spectroscopy was recorded with a DXR Raman microscope (Thermo

Scientific) under 455 nm diode laser excitation. The X-ray photoelectron spectroscopy (XPS) of the sample was recorded on Thermo Scientific K-Alpha with Al Kα rays (hv=1486.6 eV). Photoluminescence (PL) was measured at room temperature using an Edinburgh FLS1000 spectrometer with a Xe lamp with a 250 nm excitation wavelength. Cathodoluminescence (CL) measurements were performed at room temperature and 10 keV electron energy using a Rainbow CL.

Electrochemical and Performance Tests. Preparation of the anode: Ga_2O_3 nanobelts nanoribbons prepared on carbon textiles substrate by DMT method were used as electrodes directly. The mass of Ga_2O_3 nanobelts deposited on carbon textiles substrate was determined by weighing the substrate before and after fabricating process. The electrochemical experiments were performed using CR2032-type coin cells. The counter electrode was a commercial lithium plate. The separator was a Celgard 2400 polypropylene membrane. The electrolyte was 1 M $LiPF_6$ in the mixture of ethylene carbonate (EC), diethyl carbonate (DEC) and dimethyl carbonate (DMC) (1:1:1 in volume ratio). The assembling of coin cells was performed in a glovebox (DuoV S-A2-I) filled with Ar. The electrochemical performance is tested with the Neware test system in the voltage range of 0.005-3.0 V. The CV performance curve is measured by CHI 660E type electrochemical workstation in the voltage range of 0.005-3.0 V (vs. Li+/Li).

REFERENCES

1. D. Dohy and G. Lucazeau, *J. Mol. Struct.*, 1982, **79**, 419-422.
2. L. Fu, Y. Liu, P. a. Hu, K. Xiao, G. Yu and D. Zhu, *Chem. Mater.*, 2003, **15**, 4287-4291.
3. K. Wang, W. Ye, W. Yin, W. Chai, B. Tang and Y. Rui, *Dalton Trans.*, 2019, **48**, 12386-12390.
4. Y. Zhu, Q.-K. Yu, G.-Q. Ding, X.-G. Xu, T.-R. Wu, Q. Gong, N.-Y. Yuan, J.-N. Ding, S.-M. Wang, X.-M. Xie and M.-H. Jiang, *Nanoscale Research Letters*, 2014, **9**, 48.
5. S. Delpeux, F. Beguin, R. Benoit, R. Erre, N. Manolova and I. Rashkov, *Eur. Polym. J.*, 1998, **34**, 905-915.
6. Q. Xu and S. Zhang, *Superlattices Microstruct.*, 2008, **44**, 715-720.
7. A. C. Ferrari, *Solid State Commun.*, 2007, **143**, 47-57.
8. X. Wei, H. Zhang, D. Sun, C. Tian, J. Guo, S. Cui and W. Tang, *Ceram. Int.*, 2020, **46**, 21172-21181.
9. P. Lefort, D. Tetard and P. Tristant, *J. Eur. Ceram. Soc.*, 1993, **12**, 123-129.
10. D. Tham, C. Y. Nam, K. Byon, J. Kim and J. E. Fischer, *Applied Physics A*, 2006, **85**, 227-231.
11. J. Yan, K. Ge, H. Li, X. Yang, J. Chen, L. Wan, J. Guo, F. Li, Y. Xu, D. Song, B. S. Flavel and J. Chen, *Nanoscale*, 2021, **13**, 11439-11445.
12. C. Meier, S. Lüttjohann, V. G. Kravets, H. Nienhaus, A. Lorke and H. Wiggers, *Physica E: Low-dimensional Systems and Nanostructures*, 2006, **32**, 155-158.
13. R. Bhujel, U. Rizal, A. Agarwal, B. S. Swain and B. P. Swain, *J. Mater. Eng. Perform.*, 2018, **27**, 2655-2660.
14. S. B. Patil, I. Y. Kim, J. L. Gunjakar, S. M. Oh, T. Eom, H. Kim and S.-J. Hwang, *ACS Appl. Mater. Interfaces*, 2015, **7**, 18679-18688.
15. Y. J. Choi, H. S. Ryu, G. B. Cho, K. K. Cho and K. W. Kim, *Journal of the Korean Electrochemical Society*, 2009, **12**.
16. Y. Huang, X. Tang, J. Wang, H. Ma, Y. Wang, W. Liu, G. Wang, L. Xiao, J. Lu and L. Zhuang, *Langmuir*, 2019, **35**, 13607-13613.
17. Z. Xu, D. Li, D. Zhang, J. Xu, J. Lu and S. Ni, *ChemElectroChem*, 2021, **8**, 3304-3310.